On-Demand Magnon Resonance Isolation in Cavity Magnonics

Amin Pishehvar,[1] Zhaoyou Wang,[2] Yujie Zhu,[3] Yu Jiang,[1] Zixin Yan,[1] Fangxin Li,[2] Josep M. Jornet,[1] Jia-Mian Hu,[3] Liang Jiang,[2] and Xufeng Zhang[1,4,*]

[1]*Department of Electrical and Computer Engineering, Northeastern University, Boston, MA 02115, USA*
[2]*Pritzker School of Molecular Engineering, University of Chicago, Chicago, IL 60637, USA*
[3]*Department of Materials Science and Engineering, University of Wisconsin - Madison, Madison, WI 53706, USA*
[4]*Department of Physics, Northeastern University, Boston, MA 02115, USA*

(Dated: January 20, 2025)

Cavity magnonics is a promising field focusing the interaction between spin waves (magnons) and other types of signals. In cavity magnonics, the function of isolating magnons from the cavity to allow signal storage and processing fully in the magnonic domain is highly desired, but its realization is often hindered by the lack of necessary tunability on the interaction. This work shows that by utilizing the collective mode of two YIG spheres and adopting Floquet engineering, magnonic signals can be switched on-demand to a magnon dark mode that is protected from the environment, enabling a variety of manipulation over the magnon dynamics. Our demonstration can be scaled up to systems with an array of magnonic resonators, paving the way for large-scale programmable hybrid magnonic circuits.

Dark mode [1] in electromagnetic devices is a phenomenon where a mode is isolated from the environment due to destructive interference or suppressed coupling. These modes often exhibit extended lifetimes because of reduced radiation emission into the environment, leading to important applications across a wide variety of platforms. For instance, in integrated photonics, dark modes are implemented in metasurfaces to achieve supercavity lasing [2–4]; in optomechanics, dark mode allows phonon-mediated quantum coupling between two optical resonators without requiring the mechanical resonator cooled down to its quantum mechanical ground state [5–8]; while for superconducting qubits or cold atoms, dark mode is used to protect delicate quantum states [9, 10].

In the emerging field of cavity magnonics [11–17], dark mode also finds important applications. Cavity magnonics studies the interaction between magnons and microwave photons in hybrid devices [18–24], with promising potential in coherent and quantum information processing [25–29]. Thanks to the large spin density in magnonic resonators, the magnon-photon coupling strength can exceed their individual dissipation, bringing the system into the strong coupling regime, where information is exchanged between magnon and photon modes multiple times before decaying to below the noise level [18, 30–32], enabling critical signal processing functionalities [33]. When multiple magnonic resonators couple with a single microwave cavity, collective magnon dark modes can form, which isolate magnons from the cavity [30, 34], allowing the information to be stored in the magnonic domain and fully processed using magnonic approaches.

To harness the full potential of magnon dark modes, on-demand dark-bright mode conversion is required. However, such mode conversion is a fundamental challenge on all physical platforms, considering the isolated nature of the dark modes. It is worth noting that such on-demand conversion is fundamentally different – and thus should be differentiated – from the fixed dark-bright mode coupling which is relatively easy to achieve [35–39]. Thus far, on-demand dark-bright mode conversion has only been demonstrated on very few systems, such as integrated photonics [40] and optomechanics [41]. In this work, we show that, for the first time, on-demand dark-bright mode conversion can be achieved on a magnetic platform. By applying Floquet engineering [42] to a multimode magnonic system, the magnon dark and bright modes can be coupled with a coupling strength determined by the amplitude and phase of a driving signal. This capability enables on-demand isolation of the giant spin ensemble from the microwave cavity, paving the way for advanced magnonic signal processing.

Our device comprises a three-dimensional (3D) microwave cavity supporting a TE_{101} mode at $\omega_c = 2\pi \times 8.3$ GHz with a quality factor of 2500 [Fig. 1(a)]. The cavity is probed by a coaxial probe via reflection measurement (S_{11}) using a vector network analyzer (VNA). Two identical yttrium iron garnet (YIG) spheres (diameter: 0.4 mm) are positioned at the bottom of the cavity, each supporting a Kittel mode at frequency $\omega_n = \gamma H_n$, where H_n is the bias magnetic field for the n-th ($n = 1, 2$) YIG sphere provided by a permanent magnet, and $\gamma = 2\pi \times 28$ GHz/T is the gyromagnetic ratio. To introduce Floquet drives to the magnon modes, a 10-turn flat coil is placed inside the cavity underneath each YIG sphere, with the coil axis parallel to the bias field direction (z direction).

This multimode Floquet cavity electromagnonic system can be described by the Hamiltonian $\hat{H}(t) = \hat{H}_0 + \hat{H}_F(t)$. The first term represents the conventional cavity electromagnonic system, which in the rotating frame of

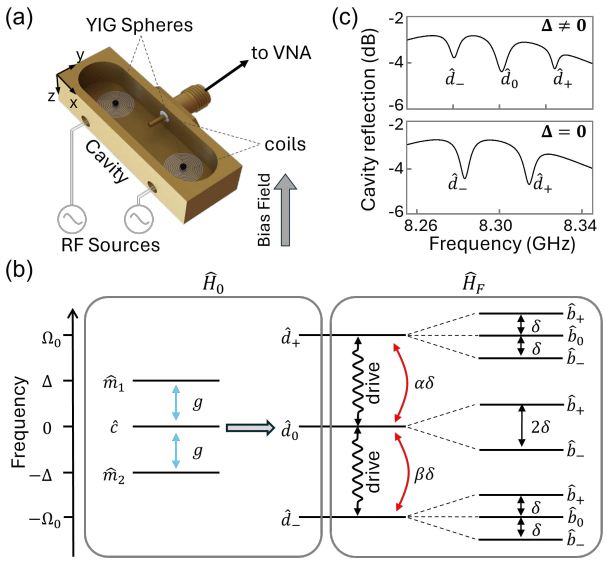

FIG. 1. (a) Device schematics. Two YIG spheres are placed at the center of two flat coils inside a copper cavity. The coils are parallel to the bias magnetic field to applying the Floquet drive. The coaxial probe is for microwave excitation and readout. (b) Energy level diagram. $\hat{m}_1(\hat{m}_2)$, first (second) magnon mode; $\hat{c}$, cavity mode; g, magnon-photon coupling strength; $\hat{d}_\pm$, upper (lower) hybrid mode; $\hat{d}_0$, center hybrid mode; $\alpha_\pm\delta$, energy level difference of $\hat{d}_0$ with $\hat{d}_\pm$; $\hat{b}_\pm$, upper (lower) Floquet hybrid mode; $\hat{b}_0$, center Floquet hybrid mode; δ, energy level difference between two Floquet hybrid modes. (c) Reflection spectra of the microwave cavity. Top: three modes ($\hat{d}_0$ and $\hat{d}_\pm$) from the hybridization of one cavity mode and two magnon modes from the two YIG spheres; bottom: the center mode ($\hat{d}_0$) becomes a dark mode and disappears when $\Delta = \omega_m - \omega_c = 0$.

the cavity mode can be represented as

$$\hat{H}_0 = \hbar \sum_{n=1,2} \left[\Delta_n \hat{m}_n^\dagger \hat{m}_n + g_n(\hat{c}^\dagger \hat{m}_n + \hat{c}\hat{m}_n^\dagger)\right], \qquad (1)$$

where $\Delta_n = \omega_n - \omega_c$ is the frequency detuning of the n-th magnon mode, g_n is the coupling strength between the n-th magnon mode and the cavity mode, $\hat{c}^\dagger$ and $\hat{c}$ ($\hat{m}_n^\dagger$ and $\hat{m}_n$) are the creation and annihiliation operators for the cavity (n-th magnon) mode, respectively. Unless explicitly mentioned, we assume $g_1 = g_2 = g$ and $\Delta_1 = -\Delta_2 = \Delta > 0$ throughout our analysis. The second term $\hat{H}_F(t)$ represent the Floquet interaction

$$\hat{H}_F(t) = \hbar \sum_{n=1,2} \epsilon_n \cos(\Omega_F t + \phi_n)\hat{m}_n^\dagger \hat{m}_n, \qquad (2)$$

where ϵ_n and ϕ_n are the amplitude and phase of the Floquet drive applied to the n-th YIG sphere, respectively. Ω_F is the frequency of the Floquet drive, which are assumed to be identical for both YIG spheres for simplicity.

The system can be illustrated by the energy level diagram in Fig. 1(b). The magnon modes (Kittel modes) of the two YIG spheres couple simultaneously to the same cavity mode, rending the two spheres an effective giant spin ensemble. In the absence of the Floquet drive, the two magnon modes form two ensemble modes $\hat{m}_\mathrm{B} = (\hat{m}_1 + \hat{m}_2)/\sqrt{2}$ and $\hat{m}_\mathrm{D} = (\hat{m}_1 - \hat{m}_2)/\sqrt{2}$. When both magnon modes are on resonance with the cavity ($\Delta = 0$), $\hat{m}_\mathrm{D}$ does not couple with the cavity mode $\hat{c}$ (thus referred to as the magnon dark mode [30]), leading to the final dark mode $\hat{d}_0 = \hat{m}_\mathrm{D}$, which cannot be observed in the cavity reflection spectrum; while $\hat{m}_\mathrm{B}$ is coupled to the cavity mode $\hat{c}$ (accordingly referred to as the magnon bright mode), forming two new normal modes $\hat{d}_\pm$ at $\omega_c \pm \Omega_0$ [Fig. 1 (c)]. Under this condition, the coupling of a single magnon mode with the cavity mode can be extracted from the splitting $g/2\pi = \Omega_0/2\sqrt{2}\pi = 12.6$ MHz. When the magnon modes are detuned ($\Delta \neq 0$), the magnon dark mode becomes "less dark" and gradually shows up in the cavity reflection spectrum.

When a Floquet drive with a frequency $\Omega_\mathrm{F} = \Omega_0$ is applied, it facilitates the interaction between the hybrid modes, as indicated by the Floquet Hamiltonian in the rotating frame of $\hat{H}_0$

$$\hat{H}_F = \delta \hat{d}_0^\dagger(\alpha \hat{d}_+ + \beta \hat{d}_-) = \delta \hat{d}_0^\dagger \hat{d}_\mathrm{B}, \qquad (3)$$

where α and β are the mixing coefficients [43]. Here $\hat{d}_\mathrm{B} = \alpha\hat{d}_+ + \beta\hat{d}_-$ originates from the superposition of $\hat{d}_+$ and $\hat{d}_-$, which is referred to as the Floquet bright mode because it couples (assisted by the Floquet drive) to the center mode $\hat{d}_0$ with a nonzero coupling strength δ, forming two new hybrid modes $\hat{b}_\pm$. In contrast, the orthogonal superposition mode $\hat{d}_\mathrm{D} = \beta^*\hat{d}_+ - \alpha^*\hat{d}_-$ does not couple with the $\hat{d}_0$ mode, and thus is referred to as the Floquet dark mode. The Floquet bright (dark) mode can also be viewed as the result of constructive (destructive) interference between the Floquet couplings from the $\hat{d}_\pm$ to the $\hat{d}_0$ mode. As a result of these interactions, mode $\hat{d}_0$ splits into two levels associated with $\hat{b}_\pm$ which are separated by 2δ (assuming $\alpha = \beta = 1$ for simplicity but without losing generalicity), while the third level $\hat{b}_0 = \hat{d}_\mathrm{D}$ disappears from the spectrum because of the cancelled coupling. Similarly, $\hat{d}_\pm$ also each splits into two levels associated with $\hat{b}_\pm$ with a separation of 2δ. However, the coupling of $\hat{d}_0$ with $\hat{d}_+$ (or $\hat{d}_-$) does not cancel for $\hat{d}_+$ mode (or $\hat{d}_-$), and therefore it can still be observed [$\hat{b}_0$ modes in Fig. 1(c)].

Figure 2 plots the measured cavity reflection spectra from a device with a nonzero magnon detuning ($\Delta > 0$). Three hybrid modes are observed at 8.32103 GHz ($\hat{d}_+$), 8.30365 GHz ($\hat{d}_0$), and 8.28434 GHz ($\hat{d}_-$). When a Floquet drive is applied to both YIG spheres, Autler-Townes (AT) splittings show up on all the three modes. As the drive frequency is tuned to match the level separation ($\Omega_\mathrm{F} = \Omega_0 = 2\pi \times 18.55$ MHz), the Floquet bright mode $\hat{d}_\mathbf{B}$ is fully hybridized with the center mode $\hat{d}_0$. Here the center mode $\hat{d}_0$ splits into two hybrid modes ($\hat{b}_\pm$), and no

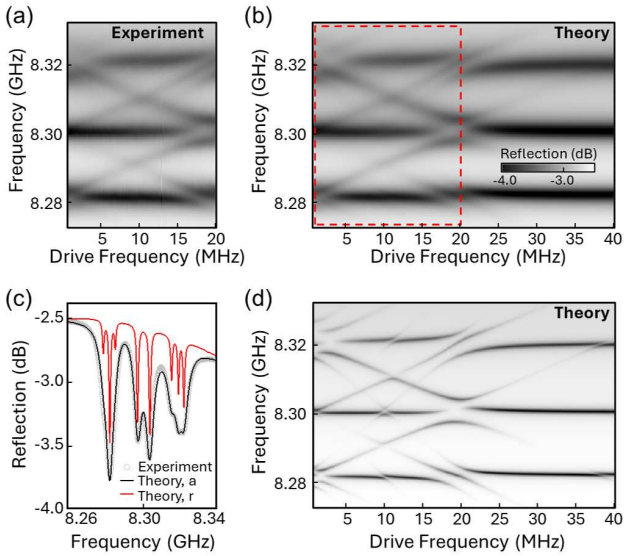

FIG. 2. (a),(b) Measured and calculated cavity reflection spectra as a function of driving frequency when both YIG spheres are driven, respectively. (c) Line plot of the measured cavity reflection (circles) and the numerical fitting (black line), together with calculation results with reduced linewidth (red). (d) Calculated cavity reflection spectra using reduced linewidth.

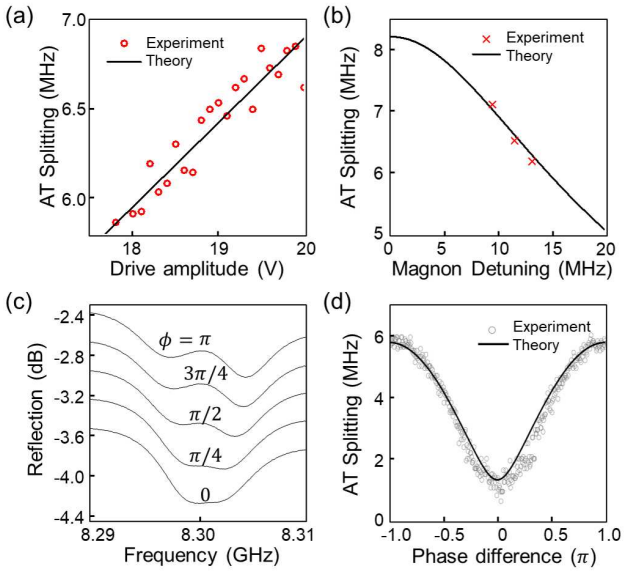

FIG. 3. (a)-(b) AT splitting as a function of the drive amplitude (here $\epsilon_1 = \epsilon_2$) and magnon detuning, respectively. (c) Measured cavity reflection spectra at different values of the phase difference ϕ between the two Floquet drives. (d) Extracted AT splitting as a function of the phase difference ϕ.

modes can be observed at the original frequency of the $\hat{d}_0$ mode, because the Floquet dark mode $\hat{d}_{\mathbf{D}}$ completely decouples with the $\hat{d}_0$ mode. Once the drive frequency shifts away from Ω_0, the two hybrids are further apart, and a center mode gradually shows up because the Floquet dark mode is no longer completely "dark".

All the experimental observation in Fig. 2(a) agrees very well with our numerical modeling (see Supplemental Materials [43] for details), as shown by the calculated spectra in Fig. 2(b). The parameters used in the calculation is obtained through numerical fitting (details see Ref. [43]), which shows excellent agreement with the measurement results [Fig. 2(c)]. Our numerical fitting reveals that the Floquet drive on Sphere 2 is 40% weaker than on Sphere 1, indicating that Sphere 2 is mounted at a larger distance from the surface of the driving coil. This can also explain the dissipation rates ($\kappa_2/2\pi = 3.1$ MHz $< \kappa_1/2\pi = 6.3$ MHz) obtained via the same numerical fitting: Sphere 1 suffers from higher losses due to closer proximity to the metallic coil. The spectra calculated using the same parameter set except for a five times reduction for all dissipation rates are also plotted [Fig. 2(d)], revealing more spectral details for the multi-mode Floquet coupling. For example, the three modes split from $\hat{d}_\pm$ become clearly visible. In addition, it also shows that the Floquet drive creates several high-order sidebands for each mode, which induce more anti-crossing features when crossing the other modes. Direct coupling between the $\hat{d}_\pm$ modes without involving $\hat{d}_0$ mode at around a drive frequency of $\Omega_F/2\pi = 38$ MHz is also observed but with much smaller splittings.

Under the dual-drive condition, the Floquet coupling strength obtained from our model is [43]

$$\delta = \frac{g\sqrt{(\epsilon_1^2+\epsilon_2^2)(g^2+\Delta^2) - 2\epsilon_1\epsilon_2 g^2\cos(\phi)}}{2(2g^2+\Delta^2)}, \quad (4)$$

where ϵ_n is the driving strength for the n-th sphere, $\phi = \phi_1 - \phi_2$ is the phase difference between the two Floquet drives, respectively. The AT splitting between the $\hat{b}_\pm$ modes equals 2δ. According to Eq. 4, the AT splitting exhibits a linear dependence on the driving amplitude ϵ. This is confirmed by the extracted AT splittings at different driving amplitudes, as shown in Fig. 3(a). When a maximum driving amplitude (4 dBm) is applied, the AT splitting reaches 6.8 MHz. This value exceeds the dissipation rates of the the interacting modes ($\kappa_0/2\pi = 2.6$ MHz, $\kappa_+/2\pi = 3.4$ MHz, $\kappa_-/2\pi = 2.55$ MHz), indicating that the Floquet-drive-induced coupling has reached the strong coupling regime. The 3-mode Floquet interaction also depends on the detuning (Δ) of the magnon modes. As the detuning reduces, the two hybrid modes $\hat{d}_\pm$ becomes closer in frequency, and accordingly it requires smaller drive frequencies. In the meantime, a larger AT splitting is achieved [crosses in Fig. 3(b)], which agrees with the theoretical prediction obtained using Eq. (4) [solid line in Fig. 3(b)].

In our experiments, the measured AT splitting shows a strong dependence on the relative phase ϕ of the two Floquet drives for the two YIG spheres [Fig. 3 (c)]. When

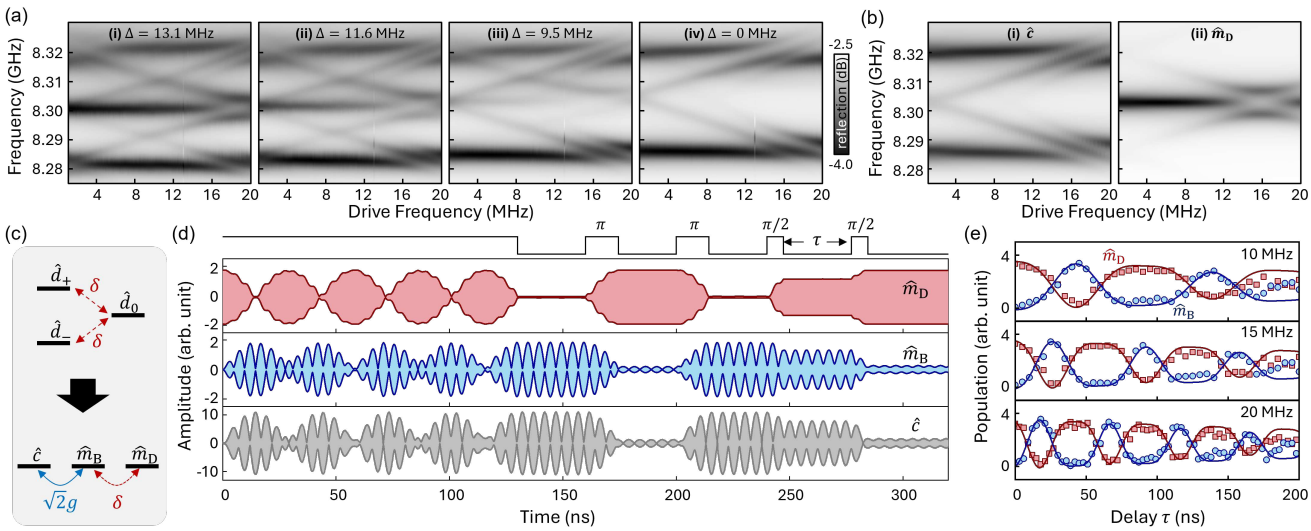

FIG. 4. (a) Measured cavity photon ($\hat{c}$ reflection spectra at different magnon detunings: $\Delta = 13.2, 11.6, 9.5, 0$ MHz, respectively. (b) Calculated spectra of the cavity photon ($\hat{c}$) and magnon dark mode ($\hat{m}_{\rm D}$) using the analytical model, respectively. (c) Effective energy diagram of the system. (d) Dynamical phase-field simulation results of the pulse response of the actual system in (a) with $\Delta = 0$ and $\Omega_F = \Omega_0$. The system is initially set to $\hat{m}_{\rm D}$ state at time 0. The top square waves show the Floquet drive pulses. (e) Magnon bright and dark mode amplitude obtained from the dynamical phase-field simulation at different drive detuning: $(\Omega_F - \Omega_0)/2\pi = 10, 15, 20$ MHz, respectively. The signal is extracted after the application of a Ramsey pulse sequence and plotted as a function of the delay between the two $\pi/2$ pulse sequence. Red squares: dark mode from simulation; blue circles: bright mode from simulation. Solid lines are from analytical calculation.

the two drives are out-of-phase ($\pm\pi$), $\hat{d}_0$ exhibits maximum AT splitting, corresponding to the constructive interference of the coupling with the two modes $\hat{d}_\pm$, where the coupling of $\hat{d}_0$ with $\hat{d}_\pm$ are in phase and add up to a stronger coupling. As ϕ decreases, the AT splitting becomes smaller, which reaches to a minimum when the two drives becomes in phase ($\phi = 0$). In this case, the coupling of $\hat{d}_0$ with $\hat{d}_\pm$ are out of phase and cancel each other, leading to diminished coupling. Such phase dependence can be conveniently explained by our model in Eq. (4). The calculated splitting is plotted as a function of ϕ [solid line in Fig. 3(d)], which shows good agreement with the experimental results. The nonzero minimum splitting at $\phi = 0$ can be attributed to the nonzero detuning of the magnon modes.

Based on the dual-mode Floquet coupling demonstrated above, controlled dark-bright mode switching can be achieved. In the spectra shown in Fig. 2(a), the detuning of the two magnon modes is not zero, and thus the center mode $\hat{d}_0$ is not a pure magnon dark mode $\hat{m}_{\rm D}$ and thus can be observed. When the magnon detuning decreases, the center mode gradually disappears, as shown in Fig. 4(a). As Δ reaches zero, the center mode $\hat{d}_0$ becomes the magnon dark mode $\hat{m}_{\rm D}$ and thus completely disappear from the spectrum [Fig. 4(a)(iv)]. However, its interaction with $\hat{d}_\pm$ still exists, as indicated by the AT splitting in the lower and upper levels. Although the AT splitting in the center mode cannot be directly measured, it can be revealed by our numerical modeling, as shown in Fig. 4(b)(ii), where a splitting is clearly visible in the center mode of the calculated spectra for the magnon dark mode $\hat{m}_{\rm D}$. The validity of our model is verified by the calculated cavity reflection spectra [Fig. 4(b)(i)] which reproduced the experimental results in Fig. 4(a)(iv) with high accuracy.

In fact, under the zero detuning condition $\Delta = 0$, mode $\hat{d}_{\rm B}$ equals $\hat{m}_{\rm B}$, and accordingly Eq. (3) reduces to $\hat{H}_F = \delta \hat{m}_{\rm D}^\dagger \hat{m}_{\rm B}$. Therefore, the effect of the Floquet drive, which induces coupling between the center mode $\hat{d}_0$ and the two modes $\hat{d}_\pm$, is equivalent to inducing the coupling between the magnon dark and bright modes [Fig. 4(c)]. In this picture, the system consists of a cavity mode $\hat{c}$, a magnon bright mode $\hat{m}_{\rm B}$, and a magnon dark mode $\hat{m}_{\rm D}$. The interaction between the cavity and magnon bright modes is constantly on (with a coupling strength of $\sqrt{2}g$), while the interaction between the magnon dark and bright modes has a strength $\delta(\epsilon)$ which is controlled by the Floquet drive ϵ. Therefore, this enables the on-demand bright-dark mode switching, allowing the isolation of the magnon modes in the two YIG spheres from the cavity as needed using an electronic signal.

To demonstrate this capability, we performed a series of time-domain dynamical phase-field simulations based on coupled Maxwell-LLG equations [44, 45], which eliminated the practical limitation of the finite magnon lifetimes. The validity of the numerical simulation is confirmed by comparison with the calculated spectra. The simulation results for a dual-sphere system with

$2\Omega_0/2\pi = 102$ MHz [which is different from Fig. 4(a)-(b)] and $\Delta = 0$ are plotted in Fig. 4(d), and more simulations details can be found in the Supplemental Materials [43]. When a continuous-wave Floquet drive is applied (0-130 ns), the switching between the magnon dark and bright modes is constantly on, causing the Rabi-like oscillation between them after the dark mode is excited at $t = 0$. The rapid oscillation between $\hat{c}$ and $\hat{m}_{\rm B}$ is due to the constantly on coupling between the two modes. When the system is in the magnon bright mode (130-160 ns), the application of a π pulse (at 160 ns) switches the system to the magnon dark mode. The system stays in the dark mode, until another π pulse (at 200 ns) switches it back to the magnon bright mode. Although the constant $\hat{c}$–$\hat{m}_{\rm B}$ coupling interferes with the magnon dark-bright mode switching, our numerical calculation shows that by properly selecting the coupling strength and Floquet drive, it is possible to completely suppress this effect [43].

Moreover, the response of the system to Ramsey pulse sequences (i.e., two $\pi/2$ pulses with a varying delay τ) is also simulated. By adjusting the detuning $(\Omega_F - \Omega_0)$ of the drive frequency in the Ramsey sequence, different interference fringes are observed [Fig. 4(e)]. As the detuning increases, the interference period becomes shorter, agreeing with the relation $T = 2\pi/(\Omega_F - \Omega_0)$. In conventional Ramsey interference experiments which typically involve two interacting modes, the system experiences a relaxation period between the two $\pi/2$ pulses. But in our three-mode system, there exists a constant interaction between the bright mode and the cavity mode. Consequently, the system stays for a shorter time in the $\hat{m}_{\rm B}$ mode than in the $\hat{m}_{\rm D}$ mode [43], exhibiting different interference fringes [Fig. 4(e)].

To conclude, this work demonstrates a controlled approach that can isolate the magnon modes from the microwave cavity. Taking advantage of the collective mode in the effective giant spin ensemble formed by a dual-YIG sphere system, magnon dark mode can be switched on using a RF drive through the Floquet process, which has been recently introduced to hybrid magnonics but limited to hybrid modes only prior to this work. Such a mechanism can be used to isolate and retrieve magnon signals from the cavity, which is one of the key functionalities that have been missing for coherent information processing in cavity magnonics. Our approach can be scaled up to more complex systems with multiple magnonic resonances, pointing to a new direction for achieving large-scale, programmable integrated magnonic circuits.

X.Z. acknowledges support from NSF (2337713) and ONR Young Investigator Program (N00014-23-1-2144). L.J. acknowledges support from the ARO (W911NF-23-1-0077), ARO MURI (W911NF-21-1-0325), AFOSR MURI (FA9550-21-1-0209, FA9550-23-1-0338), NSF (ERC-1941583, OMA-2137642, OSI-2326767, CCF-2312755), Packard Foundation (2020-71479). The dynamical phase-field simulations in this work are supported by the US Department of Energy, Office of Science, Basic Energy Sciences, under Award Number DE-SC0020145 as part of the Computational Materials Sciences Program (Y.Z. and J.-M.H.). The dynamical phase-field simulations were performed using Bridges at the Pittsburgh Supercomputing Center through allocation TG-DMR180076 from the Advanced Cyberinfrastructure Coordination Ecosystem: Services & Support (ACCESS) program, which is supported by NSF Grants No. 2138259, No. 2138286, No. 2138307, No. 2137603, and No. 2138296. J.M.J acknowledges support from AFOSR (FA9550-23-1-0254).

* xu.zhang@northeastern.edu

[1] H. Benisty, J. Opt. Soc. Am. B, JOSAB **26**, 718 (2009).
[2] M. V. Rybin, K. L. Koshelev, Z. F. Sadrieva, K. B. Samusev, A. A. Bogdanov, M. F. Limonov, and Y. S. Kivshar, Phys. Rev. Lett. **119**, 243901 (2017).
[3] M. Rybin and Y. Kivshar, Nature **541**, 164 (2017).
[4] A. Kodigala, T. Lepetit, Q. Gu, B. Bahari, Y. Fainman, and B. Kanté, Nature **541**, 196 (2017).
[5] C. Dong, V. Fiore, M. C. Kuzyk, and H. Wang, Science **338**, 1609 (2012).
[6] Y.-D. Wang and A. A. Clerk, Phys. Rev. Lett. **108**, 153603 (2012).
[7] Y.-D. Wang and A. A. Clerk, New J. Phys. **14**, 105010 (2012).
[8] D.-G. Lai, X. Wang, W. Qin, B.-P. Hou, F. Nori, and J.-Q. Liao, Phys. Rev. A **102**, 023707 (2020).
[9] M. Zanner, T. Orell, C. M. F. Schneider, R. Albert, S. Oleschko, M. L. Juan, M. Silveri, and G. Kirchmair, Nat. Phys. **18**, 538 (2022).
[10] D. H. White, S. Kato, N. Német, S. Parkins, and T. Aoki, Phys. Rev. Lett. **122**, 253603 (2019).
[11] B. Z. Rameshti, S. V. Kusminskiy, J. A. Haigh, K. Usami, D. Lachance-Quirion, Y. Nakamura, C.-M. Hu, H. X. Tang, G. E. Bauer, and Y. M. Blanter, Physics Reports **979**, 1 (2022).
[12] M. Harder and C.-M. Hu, Solid State Physics **69**, 47 (2018).
[13] D. Lachance-Quirion, Y. Tabuchi, A. Gloppe, K. Usami, and Y. Nakamura, Appl. Phys. Express **12**, 070101 (2019).
[14] B. Bhoi and S.-K. Kim, in *Solid State Physics*, Vol. 71 (Elsevier, 2020) pp. 39–71.
[15] Y. Li, W. Zhang, V. Tyberkevych, W.-K. Kwok, A. Hoffmann, and V. Novosad, J. Appl. Phys. **128**, 10.1063/5.0020277 (2020).
[16] D. D. Awschalom, C. R. Du, R. He, F. J. Heremans, A. Hoffmann, J. Hou, H. Kurebayashi, Y. Li, L. Liu, V. Novosad, J. Sklenar, S. E. Sullivan, D. Sun, H. Tang, V. Tyberkevych, C. Trevillian, A. W. Tsen, L. R. Weiss, W. Zhang, X. Zhang, L. Zhao, and C. W. Zollitsch, IEEE Transactions on Quantum Engineering **2**, 1 (2021).
[17] X. Zhang, Materials Today Electronics **5**, 100044 (2023).
[18] X. Zhang, C.-L. Zou, L. Jiang, and H. X. Tang, Phys. Rev. Lett. **113**, 156401 (2014).
[19] Y. Tabuchi, S. Ishino, T. Ishikawa, R. Yamazaki, K. Usami, and Y. Nakamura, Phys. Rev. Lett. **113**, 083603

(2014).
[20] M. Goryachev, W. G. Farr, D. L. Creedon, Y. Fan, M. Kostylev, and M. E. Tobar, Phys. Rev. Appl. **2**, 054002 (2014).
[21] L. Bai, M. Harder, Y. P. Chen, X. Fan, J. Q. Xiao, and C.-M. Hu, Phys. Rev. Lett. **114**, 227201 (2015).
[22] Y. Li, T. Polakovic, Y.-L. Wang, J. Xu, S. Lendinez, Z. Zhang, J. Ding, T. Khaire, H. Saglam, R. Divan, J. Pearson, W.-K. Kwok, Z. Xiao, V. Novosad, A. Hoffmann, and W. Zhang, Phys. Rev. Lett. **123**, 107701 (2019).
[23] J. T. Hou and L. Liu, Phys. Rev. Lett. **123**, 107702 (2019).
[24] Z.-Q. Wang, Y.-P. Wang, J. Yao, R.-C. Shen, W.-J. Wu, J. Qian, J. Li, S.-Y. Zhu, and J. Q. You, Nat. Commun. **13**, 1 (2022).
[25] Y. Tabuchi, S. Ishino, A. Noguchi, T. Ishikawa, R. Yamazaki, K. Usami, and Y. Nakamura, Science **349**, 405 (2015).
[26] D. Lachance-Quirion, S. P. Wolski, Y. Tabuchi, S. Kono, K. Usami, and Y. Nakamura, Science **367**, 425 (2020).
[27] D. Lachance-Quirion, Y. Tabuchi, S. Ishino, A. Noguchi, T. Ishikawa, R. Yamazaki, and Y. Nakamura, Sci. Adv. **3**, 10.1126/sciadv.1603150 (2017).
[28] S. P. Wolski, D. Lachance-Quirion, Y. Tabuchi, S. Kono, A. Noguchi, K. Usami, and Y. Nakamura, Phys. Rev. Lett. **125**, 117701 (2020).
[29] D. Xu, X.-K. Gu, H.-K. Li, Y.-C. Weng, Y.-P. Wang, J. Li, H. Wang, S.-Y. Zhu, and J. Q. You, Phys. Rev. Lett. **130**, 193603 (2023).
[30] X. Zhang, C.-L. Zou, N. Zhu, F. Marquardt, L. Jiang, and H. X. Tang, Nat. Commun. **6**, 1 (2015).
[31] T. Wolz, A. Stehli, A. Schneider, I. Boventer, R. Macêdo, A. V. Ustinov, M. Kläui, and M. Weides, Commun. Phys. **3**, 1 (2020).
[32] M. Song, T. Polakovic, J. Lim, T. W. Cecil, J. Pearson, R. Divan, W.-K. Kwok, U. Welp, A. Hoffmann, K.-J. Kim, V. Novosad, and Y. Li, arXiv 10.48550/arXiv.2309.04289 (2023), 2309.04289.
[33] J. Xu, C. Zhong, X. Han, D. Jin, L. Jiang, and X. Zhang, Phys. Rev. Lett. **126**, 207202 (2021).
[34] Y. Li, V. G. Yefremenko, M. Lisovenko, C. Trevillian, T. Polakovic, T. W. Cecil, P. S. Barry, J. Pearson, R. Divan, V. Tyberkevych, C. L. Chang, U. Welp, W.-K. Kwok, and V. Novosad, Phys. Rev. Lett. **128**, 047701 (2022).
[35] W. Cao, R. Singh, C. Zhang, J. Han, M. Tonouchi, and W. Zhang, Appl. Phys. Lett. **103**, 101106 (2013).
[36] X. Zhang, Q. Xu, Q. Li, Y. Xu, J. Gu, Z. Tian, C. Ouyang, Y. Liu, S. Zhang, X. Zhang, J. Han, and W. Zhang, Sci. Adv. **2**, 10.1126/sciadv.1501142 (2016).
[37] S. R. K. Rodriguez, A. Abass, B. Maes, O. T. A. Janssen, G. Vecchi, and J. Gómez Rivas, Phys. Rev. X **1**, 021019 (2011).
[38] S. Panaro, A. Nazir, C. Liberale, G. Das, H. Wang, F. De Angelis, R. Proietti Zaccaria, E. Di Fabrizio, and A. Toma, ACS Photonics **1**, 310 (2014).
[39] F. Meng, F. Meng, L. Cao, L. Cao, A. Karalis, H. Gu, M. D. Thomson, H. G. Roskos, and H. G. Roskos, Opt. Express **31**, 39624 (2023).
[40] M. Zhang, C. Wang, Y. Hu, A. Shams-Ansari, T. Ren, S. Fan, and M. Lončar, Nat. Photonics **13**, 36 (2019).
[41] D. P. Lake, M. Mitchell, B. C. Sanders, and P. E. Barclay, Nat. Commun. **11**, 1 (2020).
[42] J. Xu, C. Zhong, X. Han, D. Jin, L. Jiang, and X. Zhang, Phys. Rev. Lett. **125**, 237201 (2020).
[43] See Supplemental Material for details about device modeling, simulation, preparation, and measurements..
[44] J. Xu, C. Zhong, S. Zhuang, C. Qian, Y. Jiang, A. Pishehvar, X. Han, D. Jin, J. M. Jornet, B. Zhen, J. Hu, L. Jiang, and X. Zhang, Phys. Rev. Lett. **132**, 116701 (2024).
[45] S. Zhuang, Y. Zhu, C. Zhong, L. Jiang, X. Zhang, and J.-M. Hu, npj Comput. Mater. **10**, 1 (2024).